Chinese Chemical Letters 33 (2022) 4008–4012

Contents lists available at ScienceDirect

Chinese Chemical Letters

journal homepage: www.elsevier.com/locate/cclet

Defective TiO_2 hollow nanospheres as photo-electrocatalysts for photo-assisted Li-O_2 batteries

Hailiang Jiao[a], Guiru Sun[a,*], Yan Wang[a], Zexu Zhang[a], Zhao Wang[a], Hairui Wang[b], Haibo Li[a,*], Ming Feng[a,*]

[a] Key Laboratory of Functional Materials Physics and Chemistry of the Ministry of Education, Jilin Normal University, Changchun 130103, China
[b] Key Laboratory of Preparation and Applications of Environmental Friendly Materials of the Ministry of Education, Jilin Normal University, Changchun 130103, China

ARTICLE INFO

Article history:
Received 16 September 2021
Revised 3 November 2021
Accepted 29 November 2021
Available online 3 December 2021

Keywords:
TiO_2
Hollow nanospheres
Oxygen vacancies
Photo-electrocatalyst
Li-O_2 battery

ABSTRACT

The large overpotential for conventional Li-O_2 batteries is an enormous challenge, which impedes their practical application. Here, we prepare a defective TiO_2 (Ov-TiO_2) hollow nanosphere as photo-electrocatalyst for photo-assisted Li-O_2 batteries to reduce the overpotential. Under illumination, the oxygen vacancies as a charge separation center contribute to the separation of electrons and holes. The generated electrons could promote reducing O_2 to Li_2O_2 during oxygen reduction reaction (ORR) process, while the generated holes are beneficial to Li_2O_2 decomposition during oxygen evolution reaction (OER) process. Additionally, the proper concentration of oxygen vacancies will decrease the recombination rate between electrons and holes. The photo-assisted Li-O_2 batteries with Ov-TiO_2-650 exhibit advanced performances, such as the low overpotential (0.70 V), the fine rate capability, and the considerable reversibility accompanied with the formation/decomposition of Li_2O_2. We expect that these results could open a new mind to design of highly efficient photo-electrocatalysts for photo-assisted Li-O_2 battery.

In recent years, rechargeable lithium-oxygen (Li-O_2) batteries have attracted considerable attention due to their high theoretical specific energy density (~3500 Wh/kg), which is considered as a promising candidate to replace Li-ion batteries [1]. A typical non-aqueous Li-O_2 battery consists of a Li anode, an organic electrolyte, and a porous cathode, which operates based on the formation and decomposition of lithium peroxide (Li_2O_2) in porous cathode during oxygen reduction reaction (ORR) and oxygen evolution reaction (OER) [2]. The discharge product Li_2O_2 with insoluble and insulating natures will deposit in the porous cathode, which could clog the mass transport channel and passivate cathode, leading to a large overpotential and then lowering the charge–discharge efficiency of Li-O_2 batteries [3].

As a direct strategy to enhance the reaction kinetics of Li-O_2 batteries, a number of electrocatalysts such as noble metals (Pt and Pd) [4] and transition metal compound (CoO [5], MoS_2 [6], TiC [7], and Co_2P [8]) have been explored to boost the reaction kinetics of Li-O_2 batteries. However, the high cost of noble metals and large voltage hysteresis of transition metal compound limit their practical applications [9]. Soluble redox mediators (RMs), as another alternative, have been introduced into electrolytes to achieve the low overpotential [10]. Unfortunately, the shuttle effect of RMs could lead to the RMs degradation and Li anode corrosion, resulting in poor cycling stability [11]. Therefore, it is significant that a new strategy is developed to accelerate the decomposition of Li_2O_2.

Recently, a photo-assisted Li-O_2 battery as a new system has been explored to reduce overpotential and improve cycle life [12]. In this system, the cathode contains a suitable semiconductor with high light harvesting capability, which can separate electrons and holes under light illumination. The generated electrons and holes are beneficial for Li_2O_2 formation and decomposition, respectively [13]. To date, some semiconductors, such as TiO_2-Fe_2O_3 [14], WO_3@g-C_3N_4 NWA [15], and Co-TABQ [16] have been reported in photo-assisted Li-O_2 batteries, which remarkably lower the overpotential and enhance the rate capability. Among various semiconductors, titanium dioxide (TiO_2) is considered as a promising photocatalyst due to its non-toxicity, cost-effectiveness, good electrochemical stability, and superior photostability [17]. Unfortunately, TiO_2 exhibits poor photo-absorption and low photoconversion efficiency in the visible light resulting from its large band gap energy [18]. It has been clearly demonstrated that introducing oxygen vacancies into TiO_2 (*i.e.*, black TiO_2) can boost its photoresponse to

* Corresponding authors.
E-mail addresses: sungr@jlnu.edu.cn (G. Sun), lihaibo@jlnu.edu.cn (H. Li), mingfeng@jlnu.edu.cn (M. Feng).

https://doi.org/10.1016/j.cclet.2021.11.086
1001-8417/

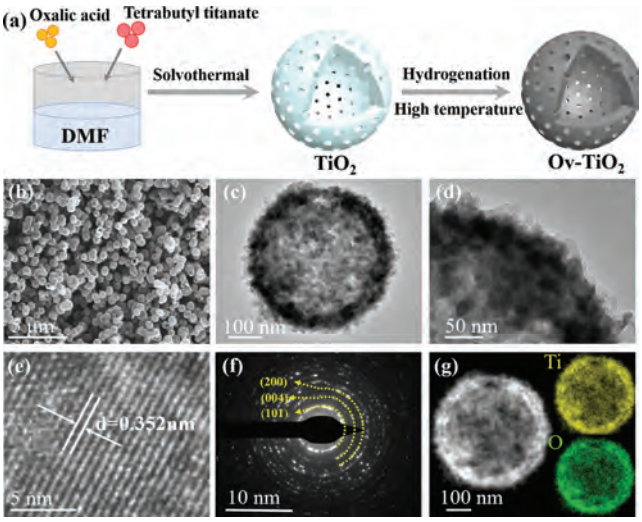

Fig. 1. (a) Schematic illustration of the preparation process of Ov-TiO_2-T, (T = 550, 600, 650 and 700). (b) SEM image, (c, d) TEM images, (e) HRTEM image, (f) SAED image, and (g) HAADF-STEM image and EDX elemental mapping images of Ov-TiO_2-650.

solar/visible light and its photocatalytic activity [19]. However, the bulk oxygen vacancies in TiO_2 will serve as recombination centers of photogenerated electrons and holes, causing the decrease of photocatalytic efficiency [20]. Therefore, it is crucial to control the concentration of oxygen vacancies on the surface of TiO_2 for improvement of its photocatalytic property.

In this work, the mesoporous TiO_2 hollow nanospheres with various concentration of oxygen vacancies (Ov-TiO_2) were synthesized at different annealing temperature, which was employed as a photo-electrocatalyst for photo-assisted Li-O_2 batteries. The oxygen vacancies as charge separation center can promote the separation of electrons and holes with illumination. The photoexcited electrons contribute to the reduction of O_2 during ORR process, while the photoexcited holes are beneficial to Li_2O_2 decomposition during OER process. Additionally, the proper concentration of oxygen vacancies will decrease the recombination rate between electrons and holes. The photo-assisted Li-O_2 batteries with Ov-TiO_2-650 exhibit a low overpotential of 0.70 V at a current density of 100 mA/g, a superior rate capability, and a good reversibility accompanied with the formation and decomposition of Li_2O_2. This work represents a promising process in the development of a highly active photo-electrocatalyst for photo-assisted Li-O_2 battery.

In Fig. 1a, the oxalic acid (10.05 g) was slowly poured into *N,N*-dimethylformamide (DMF, 90 mL) and stirred at room temperature for 30 min. Afterwards, tetrabutyl titanate (150 μL) was added into the above solution and stirred for 30 min. The obtained solution (30 mL) was then transferred to a Teflon lined autoclave with a capacity of 50 mL for a hydrothermal treatment at 170 °C for 8 h. The formed precipitate was filtered, rinsed and dried in air at 80 °C for 24 h. The obtained white product was named P-TiO_2. According to the oxygen vacancies that form under H_2 reduction, Ov-TiO_2-T (T = 550, 600, 650 and 700) were obtained by annealing pristine TiO_2 at 550, 600, 650 and 700 °C under Ar-H_2 (volume ratio of 92:8) atmosphere with a heating rate of 5 °C/min for 7 h, respectively. In comparison, TiO_2-650 is acquired after calcining at 650 °C in air for 7 h.

The morphology of P-TiO_2, TiO_2-650, and Ov-TiO_2-T (T = 550, 600, 650 and 700) were characterized by scanning electron microscope (SEM) and transmission electron microscope (TEM). In Fig. 1b and Fig. S1a (Supporting information), the P-TiO_2, TiO_2-650 and Ov-TiO_2-T (T = 550, 600, 650, and 700) are uniform nanospheres with diameter of ~500 nm. The as-prepared TiO_2 nanospheres present a hollow structure (Fig. 1c and Fig. S1b in Supporting information). In Fig. 1d and Fig. S1c (Supporting information), it can be observed that the as-prepared TiO_2 nanospheres exhibit porous structures [21]. The N_2 adsorption/desorption isotherms indicate that as-prepared TiO_2 nanospheres are mesoporous structure with a pore size distribution from 5 nm to 20 nm (Fig. S2 in Supporting information). Note that the morphology and size of Ov-TiO_2-T (T = 550, 600, 650 and 700) are similar with P-TiO_2, implying that the introduced oxygen vacancies do not alter the microstructure of TiO_2. The high-resolution transmission electron microscopy (HRTEM) images of as-prepared TiO_2 show the lattice fringes with distances of 0.35 nm, which corresponds to the (101) lattice plane of anatase TiO_2 (JCPDS #PDF No. 21-1272) (Fig. 1e and Fig. S1d in Supporting information). Interestingly, with the increasing of temperature, the distance of lattice plane is increased, which might be caused by the regrowth of grain [22]. As shown in Fig. 1f and Fig. S1e (Supporting information), the selected area electron diffraction (SAED) of as-prepared TiO_2 display (101), (004), and (200) planes, proving the polycrystalline nature [23,24]. The high-angle annular dark-field scanning TEM (HAADF-STEM) images and the corresponding energy dispersive X-ray (EDX) elemental mapping images for as-prepared TiO_2 are exhibited in Fig. S1f (Supporting information) and Fig. 1g, which clearly confirms the existence and homogeneous distribution of Ti and O elements. The atomic ratios of O and Ti are 1.88, 1.57, 1.54 and 1.56 for Ov-TiO_2-T (T = 550, 600, 650 and 700), respectively, suggesting a larger concentration of oxygen vacancies for Ov-TiO_2-650 than that of others (Table S1 in Supporting information).

Fig. 2a displays the X-ray diffraction (XRD) patterns of as-prepared P-TiO_2, TiO_2-650, and Ov-TiO_2-T (T = 550, 600, 650 and 700). The detected diffraction peaks at 25.2°, 37.8°, 48.0°, 53.9°, 55.0°, 62.7°, 68.7°, 70.3° and 75.0° are assigned to the (101), (004), (200), (105), (211), (204), (116), (220), and (215) crystal planes of anatase TiO_2 (JCPDS #PDF No. 21-1272) [25]. Raman spectra of as-prepared TiO_2 show five peaks at 167, 198, 396, 518 and 636 cm^{-1}, which are attributed to the E_{g1}, E_{g2}, B_{1g}, A_{1g} and E_{g3} Raman active modes of the anatase TiO_2, respectively (Fig. 2b). With the increases of hydrogen reduction temperature, the peak of E_{g1} shift to smaller wavenumbers (Fig. S3 in Supporting information), resulting from the charge transfer of surface disorder between O^{2-} and Ti^{4+}, further suggesting that the oxygen vacancy and Ti^{3+} exists in the as-prepared Ov-TiO_2 [26]. Note that the Ov-TiO_2-700 is an exception, which mainly because when the temperature rises to 700 °C, more energy separated electrons from oxygen vacancies and transferred to Ti^{4+} [27].

The chemical state of the TiO_2-650 and Ov-TiO_2-650 are characterized by X-ray photoelectron spectroscopy (XPS). The survey spectra exhibit that TiO_2-650 and Ov-TiO_2-650 consist of Ti and O elements (Fig. S4 in Supporting information), which agrees with the results of the above EDX mapping. The Ti 2p spectra of TiO_2-650 and Ov-TiO_2-650 are displayed in Fig. 2c. The peaks at 458.82 and 464.58 eV represent Ti^{4+}. While the peaks at 458.05 and 463.75 eV are a characteristic of Ti^{3+}. In Fig. 2d, the O 1s spectra of TiO_2-650 and Ov-TiO_2-650 show two peaks at 532.25 and 530.13 eV, which is characteristic of the lattice oxygen (O-Ti) and hydroxyl group and/or surface adsorbed oxygen, respectively [28,29]. Note that the ratio of adsorbed oxygen significantly enhances by H_2 reduction, demonstrating that oxygen vacancies is beneficial to improving surface adsorption of oxygen species [30]. Equally, the atomic ratios of O and Ti are calculated, as shown in Table S2 (Supporting information). The results show that the Ov-TiO_2-650 possesses highest concentration of oxygen vacancies, which is consistent with the EDX mapping results. The electron spin resonance (ESR) spectra of TiO_2-650 and Ov-TiO_2-650 are obtained at room temperature to determine unpaired electrons in

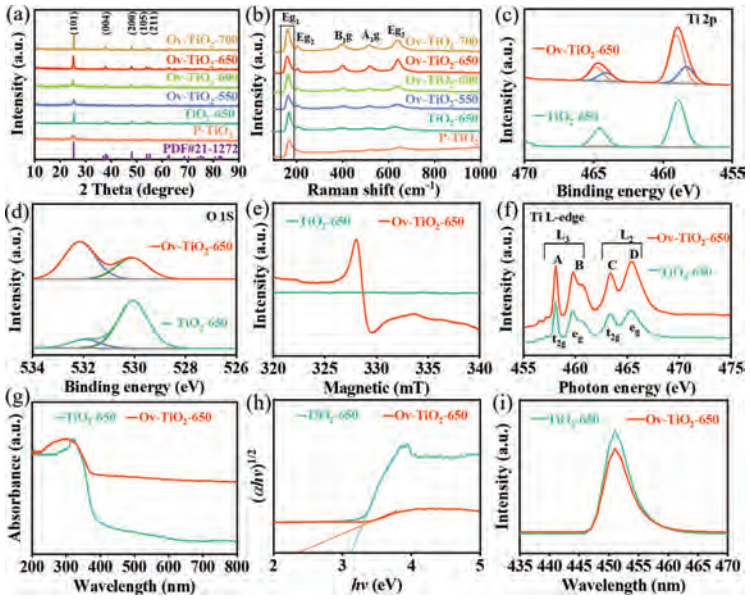

Fig. 2. (a) XRD patterns and (b) Raman spectra of as-prepared P-TiO_2, TiO_2-650, and Ov-TiO_2-T (T = 550, 600, 650 and 700). XPS core-level spectra of (c) Ti 2p and (d) O 1s of TiO_2-650 and Ov-TiO_2-650. (e) ESR spectra, (f) Ti L-edge XAS profiles, (g) UV–vis absorption spectra, (h) the corresponding Kubelke-Munk transformed diffuse reflectance spectra, and (i) PL spectra of TiO_2-650 and Ov-TiO_2-650.

oxygen vacancies [31]. As shown in Fig. 2e, the TiO_2-650 only presents a baseline noise signal, while the Ov-TiO_2-650 exhibits an unpaired electron signal at g = 2.0014, revealing the existence of oxygen vacancies in Ov-TiO_2-650. The Ti L-edge X-ray absorbtion spectrum (XAS) profiles of TiO_2-650 and Ov-TiO_2-650 are shown in Fig. 2f, which display four well-defined peaks (labeled as A, B, C and D), representing the transitions from Ti 2p to Ti 3d levels of $2p_{3/2}\rightarrow 3d\ t_{2g}$, $2p_{3/2}\rightarrow 3d\ e_g$, $2p_{1/2}\rightarrow 3d\ t_{2g}$, and $2p_{1/2}\rightarrow 3d\ e_g$, respectively. The peak of B is split into two signals due to distortion of the octahedron formed by the ligands in TiO_2 [32–34]. Generally, the intensity of characteristic peaks relates the Ti valence state. The $I(L_2)/I(L_3)$ intensity ratio for TiO_2-650 and Ov-TiO_2-650 is 1.266 and 0.692, respectively, further suggesting a high concentration of Ti^{3+} ions in Ov-TiO_2-650.

In Fig. 2g, the ultraviolet visible spectrophotometer (UV–vis) absorption spectra are used to identify the optical absorption properties of the TiO_2-650 and Ov-TiO_2-650. In comparison with the TiO_2-650, the Ov-TiO_2-650 exhibits a clearly shift in the onset of absorption from the UV to visible light region. In Fig. 2h, the bandgap of Ov-TiO_2-650 is about 2.38 eV, which is smaller than that of TiO_2-650 (3.16 eV), indicating that the solar-driven photocatalytic activity of TiO_2 can be enhanced by introducing oxygen vacancies [35]. Equally, the photoluminescence (PL) spectra are carried out to evaluate the recombination behavior of the photogenerated carriers in the TiO_2-650 and Ov-TiO_2-650 (Fig. 2i). the emission peak for the Ov-TiO_2-650 is much lower than that for TiO_2-650, demonstrating that the introducing oxygen vacancies into TiO_2 contributes to decrease the electron-hole recombination rate [36,37].

The catalytic activity of as-prepared TiO_2 is studied by evaluating the electrochemical performance of photo-assisted Li-O_2 batteries with TiO_2-650 and Ov-TiO_2-T (T = 550, 600, 650 and 700). In Fig. 3a, under illumination, the Li-O_2 cell with Ov-TiO_2-650 delivers highest discharge and charge specific capacities at 500 mA/g, which reaches 9390 and 9853 mAh/g, respectively. Note that the cells show two platforms during the charging process. The first platform at ~3.75 V is attributed to the decomposition of Li_2O_2. The second platform located at ~4.40 V, corresponding to the decomposition of electrolyte. Fig. S5a (Supporting information) displays the first discharge-charge profiles of Li-O_2 cells with TiO_2-650 and Ov-TiO_2-T (T = 550, 600, 650 and 700) at 500 mA/g under the fixed capacity of 1000 mAh/g with illumination. The discharge and charge voltage platform for a cell with Ov-TiO_2-650 are 2.80 and 3.75 V, respectively, leading to an overpotential of 0.95 V, which lower than that of Li-O_2 cells with TiO_2-650 and Ov-TiO_2-T (T = 550, 600, 700). Therefore, the Ov-TiO_2-650 could be considered to contain the proper concentration of oxygen vacancies on its surface in this work, which could decrease the recombination rate between electrons and holes [38,39].

The Li-O_2 batteries based on the Ov-TiO_2-650 are tested to study the impact of the illumination on cell performance in the discharge process. The first discharge-charge curves for the Li-O_2 batteries at 100 mA/g under a capacity limit of 1000 mAh/g with and without illumination are presented in Fig. 3b. Under illumination, the discharge potential increases from 2.72 V to 2.86 V and the charge potential decreases from 3.8 V to 3.56 V. The reduced discharge and charge overpotentials with illumination are attributed to the photo-energy [40]. Additionally, the rate performance was measured at different current densities, as shown in Fig. 3c and Fig. S5b (Supporting information). In Fig. 3c, the discharge–charge voltage plateau for a cell cycled with illumination are slightly changed from 2.86/3.56 V at 100 mA/g to 2.82/3.77 V at 500 mA/g. In contrast, the discharge voltage plateau for a cell cycled without illumination significantly decreases to 2.70 V, and the charge voltage increases to 4.01 V, at a high current density of 500 mA/g (Fig. S5b). Moreover, the cycle abilities of the cells were investigated at current density of 500 mA/g with a capacity limit of 1000 mAh/g. As shown in Fig. S6 (Supporting information), the cell shows a good cyclability of 100 cycles with illumination. For the cell without illumination, it only sustains 62 cycles. These results imply that the Ov-TiO_2-650 as photo-electrocatalysts in photo-assisted Li-O_2 battery not only contributes to the Li_2O_2 formation at a high discharge voltage but also promotes its decomposition at a low charge voltage [41].

The reversibility of Li-O_2 cells using Ov-TiO_2-650 catalyst with and without illumination is investigated through characterizing the cathodes at different electrochemical states by SEM and *in situ* XRD. In Fig. S7 (Supporting information), the super P (SP) parti-

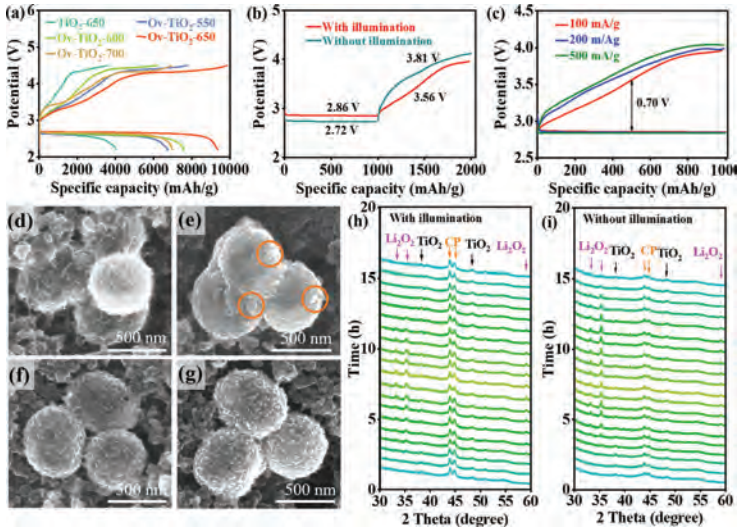

Fig. 3. (a) The discharge–charge curves of photo-assisted rechargeable Li-O_2 battery with TiO_2-650 and Ov-TiO_2-T (T = 550, 600, 650 and 700) at 500 mA/g within a potential range of 2.2–4.4 V *vs.* Li/Li^+. (b) The first discharge-charge profiles of Li-O_2 cells with Ov-TiO_2-650 with and without illumination at 100 mA/g. (c) The first discharge–charge profiles of photo-assisted Li-O_2 cell with Ov-TiO_2-650 with at different densities. SEM images of Ov-TiO_2-650 after discharge (d) without and (e) with illumination. SEM images of Ov-TiO_2-650 after recharge (f) with and (g) without illumination. *In situ* XRD patterns of Li-O_2 cell (h) with and (i) without illumination.

cles and Ov-TiO_2-650 nanospheres are distributed on the surface of cathode. After discharge, the film-like discharge product deposits on the surface of Ov-TiO_2-650 without illumination (Fig. 3d). Note that the large film-like products on the surface of catalyst limit the contact between electrolyte and active sites, which hinders the further discharge–charge reactions [14]. In contrast, under illumination, toroidal-like discharge product forms on the surface of Ov-TiO_2-650 (Fig. 3e). After recharge, some residues of film-like product remain without illumination (Fig. 3f), while the toroidal-like products totally disappear with illumination (Fig. 3g), suggesting a good reversibility of Li-O_2 cells with Ov-TiO_2-650 under illumination. Equally, the morphology of discharge products was studied after deep discharge. In Fig. S8 (Supporting information), the morphology of the discharge products remained unchanged with and without illumination. In Fig. S9 (Supporting information), after discharge, the cathodes were characterized by Raman. The peaks of Li_2O_2 at 788 cm^{-1} are observed for cathodes cycled with and without illumination, indicating that the toroidal-like and film-like discharge products are Li_2O_2. Figs. 3h and i display the *in situ* XRD patterns of Li-O_2 cells using Ov-TiO_2-650 catalyst cycled with and without illumination, respectively. The new diffraction peaks corresponding to Li_2O_2 appear and gradually increase with the discharge reaction for both cells, which proves the film-like and toroidal-like products are Li_2O_2. During recharge process, the intensity of Li_2O_2 diffraction peaks gradually decreases until it disappears for a cell cycled with illumination (Fig. 3h). In contrast, the Li_2O_2 diffraction peaks always exist after recharge for a cell cycled without illumination (Fig. 3i) [42,43]. The results further confirm the photo-assistance could improve the reversibility of Li-O_2 cells with Ov-TiO_2-650, which are consistent with the above SEM results. Additionally, the Nyquist plots of the cells using Ov-TiO_2-650 catalyst before and after cycling without and with illumination are shown in Figs. S10a and b (Supporting information). In Fig. S10c (Supporting information), the corresponding impedances are obtained by fitting using the equivalent circuit. After 2nd cycles, the total resistance value is 154.12 Ω for a cell cycled without illumination, which significantly higher than that of a cell cycled with illumination (108.89 Ω). These results reveal that a cell using Ov-TiO_2-650 catalyst with illumination exhibits a better reversibility than without illumination, providing an evidence of the high ORR and OER actives of Ov-TiO_2-650 induced by both photo-assistance and oxygen vacancies [39].

The ORR and OER performances with and without illumination are studied to verify the discharge/charge reaction mechanisms for photo-assisted Li-O_2 batteries with Ov-TiO_2-650. The cyclic voltammetry (CV) curves for the Li-O_2 cells using Ov-TiO_2-650 catalyst at 0.5 mV/s with and without illumination are exhibited in Fig. 4a and Fig. S11 (Supporting information). Compared with a cell without illumination, a higher onset reduction potential and a larger cathodic current are found for a cell under illumination. The rate capability of the Li-O_2 cells with Ov-TiO_2-650 from 50 mA/g to 1000 mA/g are studied, as shown in Fig. 4b. The cell maintained a high discharge voltage (2.71 V) at a large current density of 1000 mA/g, which clearly exceed the cell without illumination (2.51 V at 1000 mA/g). These results indicate Ov-TiO_2-650 with a higher activity toward ORR under illumination, which could be attributed to the photogenerated electrons [44,45]. Additionally, the kinetic properties of Ov-TiO_2-650 with illumination during the charge process are assessed by executing a Li_2O_2 contained experiment. The preloaded Li_2O_2 cathodes are made based on the commercial Li_2O_2 and Ov-TiO_2-650. Fig. 4c presents the linear sweep voltammetry (LSV) curves for the Li-O_2 batteries utilizing preloaded Li_2O_2 cathodes with and without illumination at a scan rate of 0.2 mV/s. It can be observed that both cells show the anodic peak related to decomposition of Li_2O_2 [14]. Significantly, the anodic peak for the cell with illumination is higher than the cell without illumination, confirming that the Ov-TiO_2-650 is beneficial to promote the decomposition of Li_2O_2 under illumination, which are consistent with the CV results (Fig. S11). This impact is further demonstrated by the constant current charging, as shown in Fig. 4d and Fig. S12 (Supporting information). The charge voltage of Li-O_2 batteries with preloaded Li_2O_2 are 3.34, 3.85, and 3.88 V at 100, 500, and 1000 mA/g, respectively with illumination, outperforming the cell without illumination. These results provide an evidence that the photo-assistance contributes to enhancing the reaction kinetics of Ov-TiO_2-650 in OER process, which could be contributed by the photogenerated holes [46,47]. In Fig. 4e, based on above experimental results, the ORR and OER mechanisms for a photo-assisted Li-O_2 batteries with Ov-TiO_2-650 are proposed. The Ov-TiO_2-650 will promote the separation of elec-

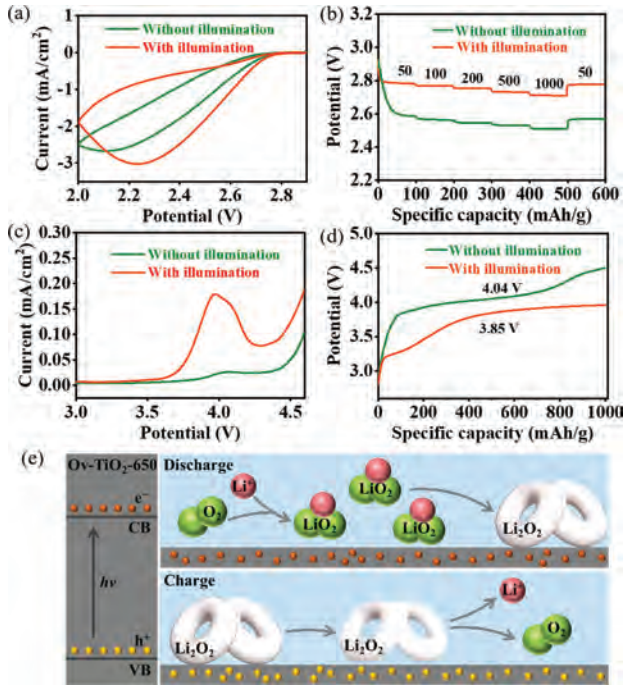

Fig. 4. (a) CV curves of Li-O_2 cells with and without illumination at 0.5 mV/s with 2.0–2.9 V *vs.* Li/Li^+. (b) Rate capability of Li-O_2 cells during the discharge process with and without illumination, (c) the LSV curves for the Li-O_2 cells with preloaded Li_2O_2 cathodes with and without illumination at 0.2 mV/s. (d) Charge curves of the Li-O_2 cells with preloaded Li_2O_2 cathodes with and without illumination at 500 mA/g. (e) Schematic diagrams of the reaction mechanisms for the photo-assisted Li-O_2 batterie with Ov-TiO_2-650.

trons and holes under illumination. During discharge process, the photoexcited electrons are uniformly distributed on surface of Ov-TiO_2-650, which could accelerate the rate of LiO_2 generation, thus facilitating the growth of Li_2O_2. During charge process, the photogenerated electrons migrate to Li anode by external circuit due to the force of the electric field, leading to the reduction of Li^+ to Li and deposition on surface of Li anode [48]. As a result, the photoexcited holes are separated to the surface of Ov-TiO_2-650, which helps to the decomposition of Li_2O_2 at a low charge voltage. Therefore, the Li-O_2 batteries with Ov-TiO_2-650 exhibit superior electrochemical performance with illumination, ascribing to appropriate a concentration of oxygen vacancies of Ov-TiO_2-650, which could provide a proper band gap and abundant active sites for the high efficiency separation of electrons and holes.

In summary, we successfully prepared the Ov-TiO_2-650 as a photo-electrocatalyst for photo-assisted Li-O_2 batteries. The Ov-TiO_2-650 presents a microstructure with abundant mesoporous channels, which could provide paths for the diffusion of Li^+ and O_2, as well as enough space for the deposition of Li_2O_2. The oxygen vacancies are as charge separation center, which contribute to the separation of electrons and holes with illumination. The photogenerated electrons are beneficial to reducing O_2 to Li_2O_2 during discharge process. Equally, the photogenerated holes could promote the decomposition of Li_2O_2 during charge process. Consequently, the photo-assisted Li-O_2 batteries with Ov-TiO_2-650 exhibit advanced performances, such as the low overpotential (0.70 V), the fine rate capability, and the considerable reversibility accompanied with the formation/decomposition of Li_2O_2. We believe that the work could offer an insight into the design of highly efficient photo-electrocatalyst for photo-assisted Li-O_2 battery.

Declaration of competing interest

The authors declare no conflicts of interests.

Acknowledgments

This work was supported by the National Natural Science Foundation of China (Nos. 21978110, 51772126, and 52171210), the Jilin Province Science and Technology Department Program (Nos. 20200201187JC, 20190201309JC, and YDZJ202101ZYTS047), the "13th five-year" Science and Technology Project of Jilin Provincial Education Department (Nos. JJKH20200407KJ and JJKH20210444KJ) and the Jilin Province Development and Reform Commission Program (No. 2020C026-3). Allocation of beamtime at 4B9B, BSRF, Beijing, China, is gratefully acknowledged. The authors would like to thank Dr. Jiaou Wang and Dr. Kaiqi Nie for the help in soft-X-ray absorption spectrum.

Supplementary materials

Supplementary material associated with this article can be found, in the online version, at doi:10.1016/j.cclet.2021.11.086.

References

[1] T. Liu, J.P. Vivek, E.W. Zhao, et al., Chem. Rev. 120 (2020) 6558–6625.
[2] Y. Dong, S. Li, S. Hong, et al., Chin. Chem. Lett. 31 (2020) 635–642.
[3] R. Gao, L. Liu, Z. Hu, et al., J. Mater. Chem. A 3 (2015) 17598–17605.
[4] Q. Liang, K. Hayashi, D. Song, ACS Catal. 10 (2020) 4895–4905.
[5] R. Gao, Z. Li, X. Zhang, et al., ACS Catal. 6 (2016) 400–406.
[6] Z. Sadighi, J. Liu, L. Zhao, et al., Nanoscale 10 (2018) 22549–22559.
[7] Y. Yang, X. Xue, Y. Qin, et al., J. Phys. Chem. C 122 (2018) 12665–12672.
[8] P. Bhanja, Y. Kim, B. Paul, et al., ChemCatChem 12 (2020) 2091–2096.
[9] W. Liu, X. Zhang, C. Li, et al., Chin. Chem. Lett. 31 (2020) 2225–2229.
[10] C. Zhu, Y. Wang, L. Shuai, et al., Chin. Chem. Lett. 31 (2020) 1997–2002.
[11] N. Feng, X. Mu, X. Zhang, et al., ACS Appl. Mater. Interfaces 9 (2017) 3733–3739.
[12] J.B. Park, S.H. Lee, H.G. Jung, et al., Adv. Mater. 30 (2018) 1704162.
[13] X.Y. Yang, X.L. Feng, X. Jin, et al., Angew. Chem. Int. Ed. 58 (2019) 16411–16415.
[14] M. Li, X. Wang, F. Li, et al., Adv. Mater. 32 (2020) e1907098.
[15] H. Xue, T. Wang, Y. Feng, et al., Nanoscale 12 (2020) 18742–18749.
[16] Y. Ni, L. Lin, Y. Shang, et al., J. Chen, Angew. Chem. Int. Ed. 60 (2021) 16937–16941.
[17] J. Choi, S. Song, M.T. Horantner, et al., ACS Nano 10 (2016) 6029–6036.
[18] Y.H. Hu, Angew. Chem. Int. Ed. 51 (2012) 12410–12412.
[19] R. Katal, M. Salehi, et al., ACS Appl. Mater. Interfaces 10 (2018) 35316–35326.
[20] M. Kong, Y. Li, X. Chen, et al., J. Am. Chem. Soc. 133 (2011) 16414–16417.
[21] Y. Chen, N. Murakami, H.Y. Chen, et al., Rare Met. 38 (2014) 468–474.
[22] W. Song, Q. Jiang, X. Xie, et al., Energy Storage Mater. 22 (2019) 441–449.
[23] S. Wang, Y. Yang, Y. Dong, et al., J. Adv. Ceram. 8 (2019) 1–18.
[24] E.S. Araújo, V.N.S. Leão, J. Adv. Ceram. 8 (2019) 238–246.
[25] Q. Ni, R. Dong, Y. Bai, et al., Energy Storage Mater. 25 (2020) 903–911.
[26] X. Pan, M.Q. Yang, X. Fu, et al., Nanoscale 5 (2013) 3601–3614.
[27] A. Sadeghzadeh-Attar, J. Adv. Ceram. 9 (2020) 107–122.
[28] J. Liu, J. Wang, Z. Ku, et al., ACS Nano 10 (2016) 1007–1016.
[29] S. Oh, J.H. Kim, H.M. Hwang, et al., J. Mater. Chem. A 9 (2021) 4822–4830.
[30] H. Gao, G. Hu, J. Sui, et al., Appl. Catal. B Environ. 226 (2018) 337–345.
[31] Y. Ma, L. Zhang, Z. Cai, et al., ACS Appl. Energy Mater. 3 (2020) 11666–11673.
[32] X. Kang, X.Z. Song, Y. Han, et al., Sci. Rep. 8 (2018) 5904.
[33] A. Paul, J.G. Zheng, T. Aoki, J. Appl. Phys. 122 (2017) 154302.
[34] Z. Zhao, D. Wang, R. Gao, et al., Angew. Chem. Int. Ed. 60 (2021) 11910–11918.
[35] G. Nechifor, E.E. Totu, A.C. Nechifor, et al., Sci. Rep. 10 (2020) 136.
[36] G. Mishra, M. Mukhopadhyay, Sci. Rep. 9 (2019) 4345.
[37] M.E. Khan, M.M. Khan, B.K. Min, et al., Sci. Rep. 8 (2018) 1723.
[38] Z. Wu, Y. Zhao, W. Jin, et al., Adv. Funct. Mater. 31 (2020) 2009070.
[39] T. Tian, L.L. Lu, Y.C. Yin, et al., Adv. Funct. Mater. 31 (2020) 2007419.
[40] K.R.G. Lim, A.D. Handoko, S.K. Nemani, et al., ACS Nano 14 (2020) 10834–10864.
[41] Z. Li, C. Zhou, J. Hua, et al., Adv. Mater. 32 (2020) e1907444.
[42] F. Sun, R. Gao, D. Zhou, et al., ACS Energy Lett. 4 (2018) 306–316.
[43] R. Gao, D. Zhou, D. Ning, et al., Adv. Funct. Mater. 30 (2020) 2001223.
[44] Y. Di, S. Jia, X. Yan, et al., N. J. Chem. 44 (2020) 791–796.
[45] J. Huang, J. Liu, J. He, et al., Angew. Chem. Int. Ed. 60 (2021) 20717–20722.
[46] C. Shu, J. Wang, J. Long, et al., Adv. Mater. 31 (2019) e1804587.
[47] A. Dutta, K. Ito, A. Nomura, et al., Adv. Sci. 7 (2020) 2001660.
[48] F. Li, J. He, J. Liu, et al., Angew. Chem. Int. Ed. 60 (2021) 6600–6608.